https://doi.org/10.26599/JAC.2024.9220898

Research Article

Investigation on crystallization behavior between $(Sc_xYb_{1-x})O_{1.5}$ and CMAS: A new insight in the effect of Sc substitution

Guangheng Zhang[a, b], Jinyu Shi[a, b], Jie Zhang[a, *], Jingyang Wang[a]

[a] Shenyang National Laboratory for Materials Science, Institute of Metal Research, Chinese Academy of Sciences, Shenyang 110016, China

[b] School of Materials Science and Engineering, University of Science and Technology of China, Shenyang 110016, China

Received: March 5, 2024; Revised: April 3, 2024; Accepted: April 14, 2024

Abstract

Environmental barrier coatings with thermomechanical robustness against calcium-magnesium-aluminum-silicate deposits are in high demand. The aim of this work is to clarify the influence of Sc^{3+} on crystallization behavior of Yb-based coatings against CMAS deposits. The reaction products of solid solutions with compositions traversing the Sc_2O_3-Yb_2O_3 system indicate that Sc^{3+} tend to form $[BO_6]$ coordination polyhedron in crystal structure to promote the formation of garnet and diopside, while Yb^{3+} occupy 7, 8 and 9-coordinate sites to crystallize apatite and silicocarnotite. The

transformation of crystalline products from apatite/silicocarnotite to garnet/diopside greatly improves the efficiency of CMAS melt consumption and facilitates the prevention of its further penetration and corrosion. Based on the commonality of cation occupancy in crystallography, an A($CaO+YbO_{1.5}$)-B($ScO_{1.5}+MgO+AlO_{1.5}$)-T(SiO_2) pseudo-ternary phase diagram is established, which has a great potential to describe phase equilibrium in coating-deposit systems and can provide guidance for compositional design of corrosion-resistant coatings.

Key words: $(Sc_xYb_{1-x})O_{1.5}$ solid solution, CMAS deposit, crystallization behavior, cation partitioning, pseudo-ternary phase diagram

∗Corresponding author: Dr Jie Zhang (email: jiezhang@imr.ac.cn)

1. Introduction

In order to improve thrust-weight ratios in aero-engine, the combustion chamber temperature continues to rise, which imposes more stringent demands on their hot-section components. Silicon carbide fiber reinforced silicon carbide ceramic matrix composites (SiC_f/SiC CMCs) with the merits of light weight, high strength and excellent resistance to high-temperature creep and oxidation, are considered to be potential candidates for the next generation aero-engine hot-section components[1]. SiC_f/SiC CMCs are suspicious in water vapor conditions with the formation of volatile silicon hydroxide, thus requires the protection of environmental barrier coatings (EBCs)[2]. With the increase in aero-engine operating temperature, material selection and structural design of EBCs face more and more challenges, one of which is the requirement for excellent stability under the attack of deposits[3]. These deposits

originate from siliceous debris such as volcanic ash, sand, dust, etc., which normally have low melting points and cause serious damage to engines at high temperatures. The widespread source of deposits leads to large differences in their composition, but the main component is a calcium-magnesium aluminum-silicate, thus commonly termed as CMAS[4].

EBCs typically exhibit lamellar or columnar microstructures, which are deposited via atmospheric plasma spraying (APS), suspension plasma spraying (SPS), plasma spray-physical vapor deposition (PS-PVD)[5]. Coating failure induced by CMAS deposits consists of two main aspects: physical penetration and chemical reaction[3, 6]. The molten CMAS tends to penetrate into intercolumnar gaps in columnar coatings or microcracks and vertical cracks in lamellar coatings, and induces a mismatched coefficient of thermal expansion (CTE) between that area and the unpenetrated coating or the substrate[7]. The mismatch generates compressive stresses in the coating interior, elevates the energy release, and eventually leads to large-area coating dehiscence and spallation[8, 9]. In contact with the CMAS melt, the dissolution of coatings and the precipitation of crystalline phases are inevitable[6]. This chemical interaction with the CMAS melt compels the coating to continuously degrade and eventually fail. Thus, EBCs with thermomechanical robustness against CMAS deposits are in high demand.

Currently, research on EBC materials mainly focused on rare earth oxide-containing materials, such as RE silicates and RE hafnates (RE = rare earth). The interaction of these coating materials with CMAS deposits crystallizes various reaction products, in which apatite and garnet are the dominant ones consuming CMAS[10, 11].

Table 1 and 2 summarized the chemical composition of apatite and garnet precipitates in CMAS corrosion of representative coatings or coating materials[12-14], in which the $REO_{1.5}$ content (14 ~ 21 mol%) in garnet is far less than that in apatite (47 ~ 50 mol%). It is obvious that garnet precipitation consumes CMAS more efficiently than apatite, under equivalent amount of coating material involved in the corrosion reaction. Meanwhile, garnet contains a higher content of alkaline constituents (CaO and MgO). It is believed that the removal of alkaline constituents from the melt effectively increases the viscosity and mitigates CMAS penetration[15, 16]. From our previous investigation, the mitigation effect of garnet precipitation on the recession of coating materials has been demonstrated in the comparison of corrosion behaviors between ytterbium oxide and ytterbium monosilicate pellets[17].

Table 1. Chemical compositions of apatite phase in CMAS corrosion of several coatings or materials

Materials-deposits	**Experiment condition**	**CaO**	**MgO**	**$AlO_{1.5}$**	**SiO_2**	**$REO_{1.5}$**	**Zr/HfO_2**	**Analysis method**
Er_2SiO_5-$Ca_{33}Mg_{10}Al_{13}Si_{44}$[12]	1400 °C-25h	13.2	—	—	37.7	49.1	—	SEM-EDS
	1300 °C-50h	12.73	—	—	39.83	47.44	—	
Yb_2SiO_5-$Ca_{33}Mg_{10}Al_{13}Si_{44}$[13]	1350 °C-50h	12.89	—	—	40.06	47.05	—	SEM-EDS
	1400 °C-50h	11.79	—	—	39.11	49.10	—	
$Yb_4Hf_3O_{12}$ -$Ca_{33}Mg_9Al_{13}Si_{45}$[14]	1300 °C-4h	12	—	—	38	49	1	TEM-EDS

Table 2. Chemical compositions of garnet phase in CMAS corrosion of several coatings or materials

Materials-deposits	**Experiment condition**	**CaO**	**MgO**	**$AlO_{1.5}$**	**SiO_2**	**$REO_{1.5}$**	**Zr/HfO_2**	**Analysis method**
Er_2SiO_5-$Ca_{33}Mg_{10}Al_{13}Si_{44}$[12]	1400 °C-25h	8.1	10.5	33.8	19.6	28.0	—	SEM-EDS

	1300 °C-50h	17.61	15.81	12.49	35.05	19.04	—	
Yb_2SiO_5-$Ca_{33}Mg_{10}Al_{13}Si_{44}$[13]	1350 °C-50h	21.29	15.04	11.07	38.35	14.26	—	SEM-EDS
	1400 °C-50h	15.73	18.51	10.96	35.79	19.01	—	
$Yb_4Hf_3O_{12}$ -$Ca_{33}Mg_9Al_{13}Si_{45}$[14]	1300 °C-4h	17	15	14	29	19	3	EPMA

The extensive investigations of interaction between rare earth silicate and various CMAS deposits indicate that the high Al^{3+} and Mg^{2+} content in the melt promotes garnet formation[10, 11, 17, 18], since Al^{3+} and Mg^{2+} satisfy the specific coordination polyhedrons in garnet crystal. However, the instability in high-temperature water vapor environment[19] and poor compatibility with silicates[20] inhibit the incorporation of aluminum and magnesium constituents into EBC systems. Sc, which exhibits a close ionic radius to Mg[21], in Table S1, could be regarded as garnet forming species according to the report of crystal chemistry by Novak et.al[22]. The high cost has resulted in limited and unsystematic researches on the CMAS corrosion behavior of $ScO_{1.5}$-containing EBCs or corresponding materials. When screening or optimizing coating materials, it is impractical to conduct experimental tests in all possible scenarios due to the wide range of optional compositions. Many investigations have focused on the phase equilibria and thermodynamic properties in the interaction of deposits with coating materials[23, 24], particularly with the rare earth element[18, 25, 26], since the crystallization behavior is strongly dependent on the rare earth constituents.

In this study, a series scandium-ytterbium oxide solid solutions $(Sc_xYb_{1-x})O_{1.5}$ ($0 \leq x \leq 1$) were prepared, mixed with model CMAS with various ratios and treated at 1300 °C to investigate their reactive crystallization behaviors under conditions relevant to the EBC-deposit interactions. It is expected that this thermodynamic investigation

favors for fundamental understanding the reaction of coating materials with CMAS deposits and the crystallization process of various reaction products.

2. Materials and Experimental methods

$(Sc_xYb_{1-x})O_{1.5}$ solid solutions with composition covering the binary system of Sc_2O_3-Yb_2O_3 (x = 0.0, 0.1, 0.2, 0.3, 0.5, 0.7, 0.9 and 1.0) and model CMAS deposit with a composition of 33CaO-9MgO-13$AlO_{1.5}$-45SiO_2 (in mole ratio) were selected in this investigation, and prepared as powders by the method of solid state reaction. $Ca_{33}Mg_9Al_{13}Si_{45}$ with a melting point of ~ 1233 ºC, originated from the average deposit composition in aero-engines exposed to desert environments[27], and approached the eutectic composition[18], which was considered as the most typical CMAS deposit. The commercial powders of scandium, ytterbium oxides (99.9% purity, Dahua New Material Resources Co., Ltd., Ganzhou, China) and calcium, magnesium, aluminum and silicon oxides (99.7% purity; Sinopharm Chemical Reagent Co. Ltd., Shanghai, China), were weighed according to the desired stoichiometries and placed into Si_3N_4 containers and ball-milled with ethanol medium for 24 h. After removing the ethanol, the mixtures were transferred to chamber furnaces. $(Sc_xYb_{1-x})O_{1.5}$ and CMAS powders were sintered at 1500 ºC for 10 h and 1150 ºC for 24 h, respectively. Sintered samples were both ball-milled again to ensure uniformity of powder particles.

The prepared $(Sc_xYb_{1-x})O_{1.5}$ and CMAS powders were blended in a molar ratio equals to 1:10 or 1:5, to obtain a series of mixtures. The selected $(Sc_xYb_{1-x})O_{1.5}$:CMAS ratios ensured both the saturation of rare earth constituents in CMAS melt to precipitate crystalline products and the surplus of CMAS melt to maintain consistency in the

quantity of rare earth constituents involved in the different reactions. The ratios of 1:10 and 1:5 were employed to simulate the crystallization behavior of reaction products at the early and later stages of CMAS corrosion, respectively. Mixtures were compacted into pellets with an 8-millimeter diameter and a 2-millimeter height, held on a monocrystalline alumina substrate plated with platinum and annealed in a chamber furnace at 1300 ºC for 1 h with a heating and cooling rate of 5 ºC/min. The platinum layer prevented alumina substrate from the erosion of molten mixtures.

X-ray diffractometer (XRD, D8 Discover, Bruker, Germany) with Cu K_α radiation was utilized to identify the phase composition. To ensure the accurate identification on phase composition of heat-treated $(Sc_xYb_{1-x})O_{1.5}$-CMAS mixtures, the samples were smashed and ground to powders before XRD measurement. The observation of morphology and determination of chemical composition were achieved by SUPRA 55 scanning electron microscope (SEM, LEO, Oberkochen, Germany) and energy-dispersive X-ray spectroscopy (EDS, X-Max, Oxford, Britain).

3. Results

3.1 Characterization of as-synthesized $(Sc_xYb_{1-x})O_{1.5}$ solid solution powders

Figure 1 aggregates XRD patterns and EDS elemental mapping of $(Sc_xYb_{1-x})O_{1.5}$ solid-solution powders with compositions $0 \leq x \leq 1$. All solid-solutions have a cubic bixbyite structure with $Ia\bar{3}$ space group. The substitution of Sc^{3+} for large-size Yb^{3+} reduces the unit cell volume and lattice constant, so the diffraction peak positions systematically shifted towards the high-angle region. From the EDS result, it is apparent that the distribution of Yb and Sc elements is homogeneous. $ScO_{1.5}$ and $YbO_{1.5}$ form

complete solid solutions over the whole range. The successful preparation of solid solutions ensures the simultaneous involvement of the scandium and ytterbium constituents in subsequent reactions with CMAS deposits, and establishes a basis for the future synthesis of corresponding coating materials.

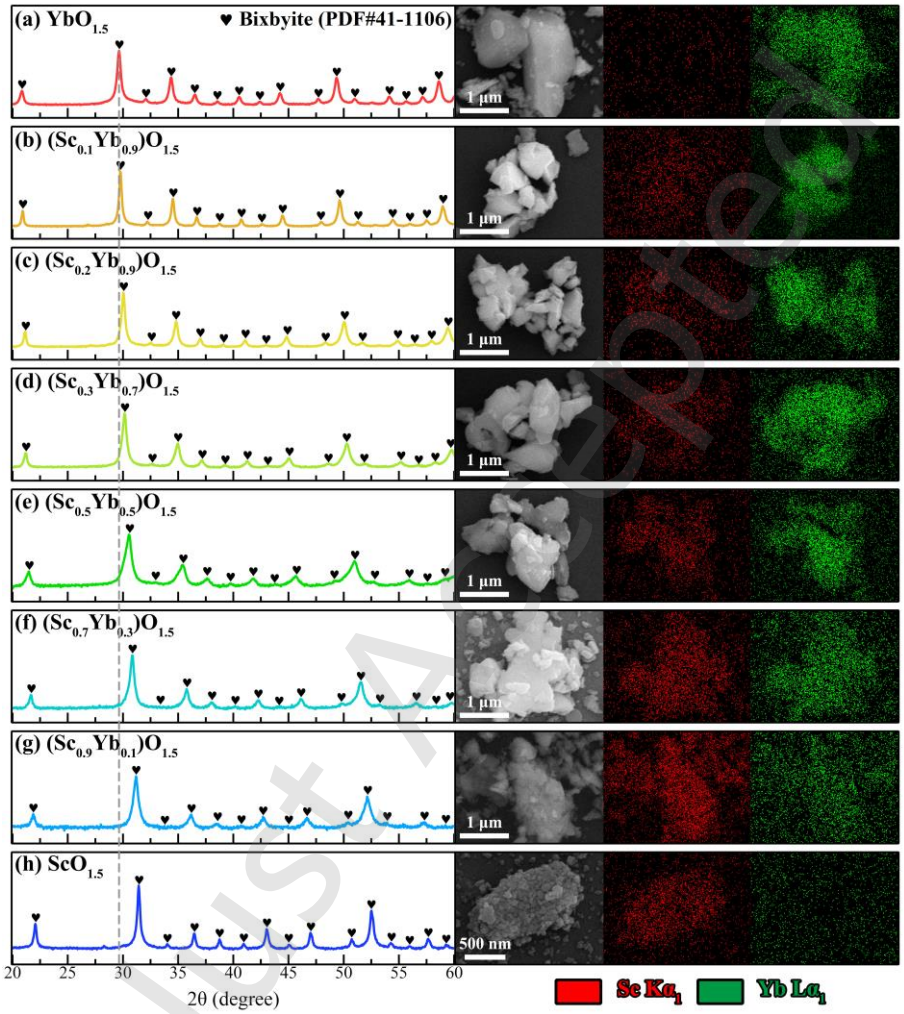

Figure 1. XRD patterns and EDS mapping of $(Sc_xYb_{1-x})O_{1.5}$ solid-solution powders with various compositions: x = 0.0, 0.1, 0.2, 0.3, 0.5, 0.7, 0.9 and 1.0, from top to bottom.

3.2 Characterization of treated $(Sc_xYb_{1-x})O_{1.5}$-CMAS mixtures

3.2.1 Microstructure and phase composition of mixtures

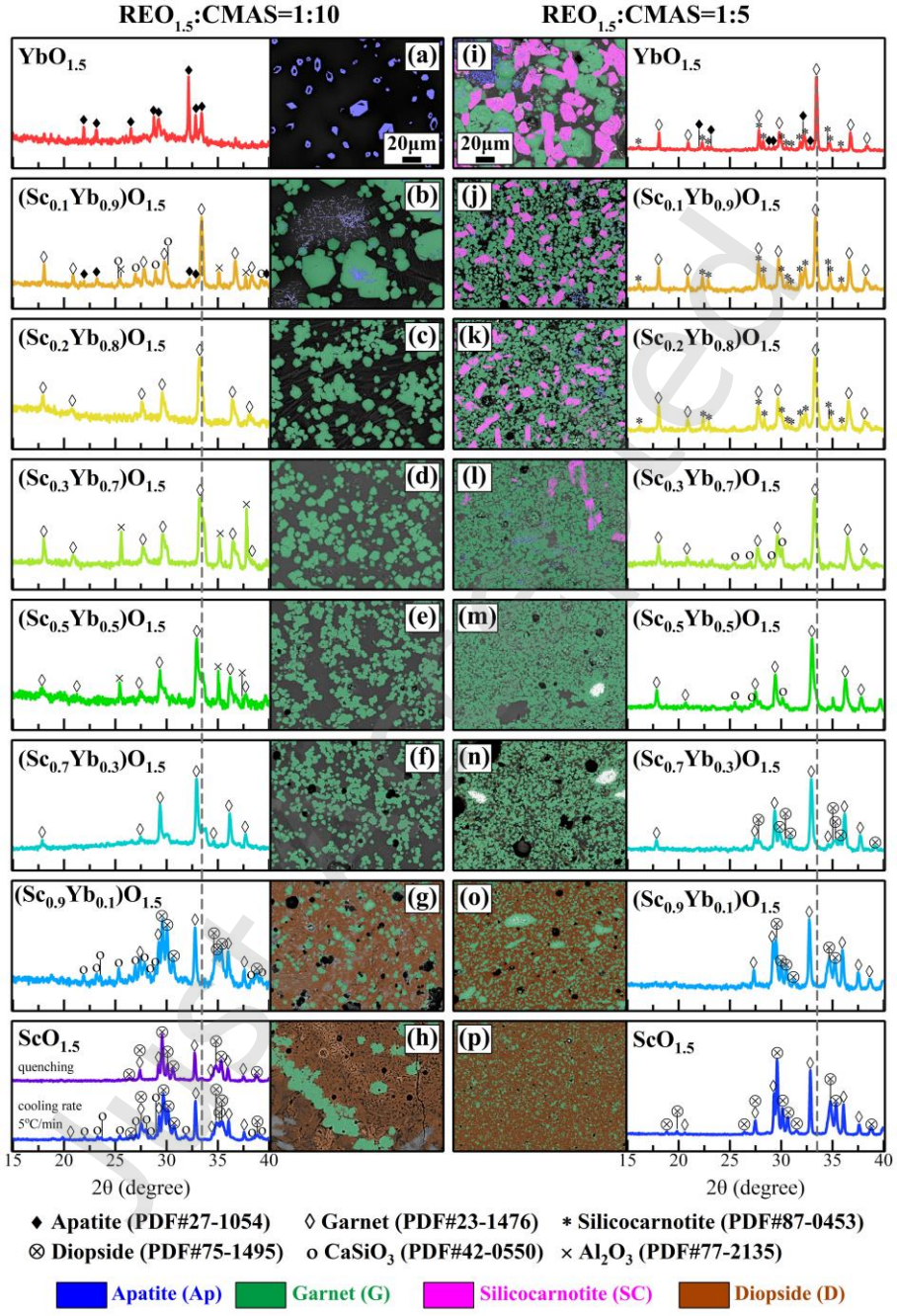

Figure 2. XRD patterns and BSE micrographs of $(Sc_xYb_{1-x})O_{1.5}$-CMAS mixtures treated at 1300 °C for 1 h.

XRD patterns and representative backscattered electron (BSE) images depict crystalline phase combinations in two mixtures with $(Sc_xYb_{1-x})O_{1.5}$:CMAS ratios of

1:10 and 1:5 after treated at 1300 ºC for 1 h, as shown in Figure 2. The reaction of $(Sc_xYb_{1-x})O_{1.5}$ solid solutions with CMAS deposits crystallizes four products: apatite, garnet, silicocarnotite and diopside. To facilitate the differentiation of four reaction products, apatite, garnet, silicocarnotite and diopside grains are filled with blue, olive green, magenta and brownish red, respectively, based on their contrasts in initial BSE images (Figure S1). In addition, diffraction peaks belonging to calcium silicate ($CaSiO_3$) and aluminum oxide (Al_2O_3) were detected in some samples (Figure 2b, d, e, g, h and l). It is found that diffraction peaks belonging to $CaSiO_3$ disappear when the mixture with a $ScO_{1.5}$:CMAS ratio of 1:10 is held at 1300 ºC for 1 h and then quenched in air. The crystallization of $CaSiO_3$ from CMAS occurs during cooling. Diffraction peaks belonging to Al_2O_3 are extremely sharp, which has been attributed to a few fragments of single-crystal substrate during the preparation of XRD samples. Meanwhile, Al_2O_3 grains are not observed in BSE micrographs. $CaSiO_3$ and Al_2O_3 will not be further discussed subsequently.

Figure 2a-h show the microstructure and phase composition of $(Sc_xYb_{1-x})O_{1.5}$ reacted with the CMAS deposit in a ratio of 1:10. Without the incorporation of $ScO_{1.5}$ constituent, the reaction of ytterbium oxide with CMAS deposit merely crystallizes apatite product (Figure 2a). In this case, the blue apatite grains occupy a small volume fraction, and the majority region in the sample is amorphous glass formed by the residual CMAS melt. The phase composition of crystalline products evolves diversely with the introduction of $ScO_{1.5}$ constituent. When the $ScO_{1.5}$ content in the solid solution reaches to 10 mol%, apatite and garnet grains are simultaneously observed in

the sample (Figure 2b). Garnet grains have a massive morphology. The considerable amount of precipitated garnet inhibits the growth of apatite, leading to a significant reduction in its grain size. When the $ScO_{1.5}$ content in the solid solution is maintained at 20 ~ 70 mol%, apatite grains are no longer observed in the sample and reaction products are exclusively garnet (Figure 2c-f). During this period, the increase in $ScO_{1.5}$ content merely affects the grain size of garnet. Once the $ScO_{1.5}$ content exceeds 90 mol%, another reaction product, diopside, precipitates (Figure 2g and 2h). The diopside crystallization consumes the CMAS melt in large quantities, thus very little residue is observed in these samples.

Figure 2i-p illustrate the microstructure and phase composition of samples with a $(Sc_xYb_{1-x})O_{1.5}$:CMAS ratio of 1:5. It is obvious that an increase in scandium-ytterbium oxide solid solution depletes the CMAS melt, and precipitates more crystalline products. These crystalline products comprise a significant volume fraction in the samples, but their phase compositions are quite distinct. For the sample with a $YbO_{1.5}$:CMAS ratio of 1:5, reaction products comprise garnet, silicocarnotite and minor apatite (Figure 2i). The introduction of $ScO_{1.5}$ constituent in these samples causes an increase in garnet and a reduction or even complete disappearance of apatite and silicocarnotite (Figure 2j-m). Diffraction peaks belonging to the diopside phase have been identified in the mixture with a $(Sc_{0.7}Yb_{0.3})O_{1.5}$ (Figure 2n), but with very low intensity. The diopside phase appears abundantly in solid solutions with $ScO_{1.5}$ content over 90 at. % (Figure 2o and 2p), and its volume fraction even exceeds that of garnet.

3.2.2 Chemical composition of crystalized products

The compositions of apatite are determined by EDS and shown in Table 3. Apatite consists of CaO, SiO_2, $YbO_{1.5}$ and $ScO_{1.5}$, and these constituents fluctuate in different samples. In contrast to the results in Table 1[12-14], the total $REO_{1.5}$ content in apatite is in the range of 38 ~ 48 mol%. Apatite crystallizes in the interaction between $(Sc_xYb_{1-x})O_{1.5}$ solid solutions with a $ScO_{1.5}$ content of 0 ~ 30 mol% and CMAS deposits (Figure 2a, b and i-l), i.e., the $ScO_{1.5}$ content in the mixture reaches to 5.0 mol%. However, the $ScO_{1.5}$ content in apatite retains stable in the range of 0.6 ~ 1.0 mol%, which is less than 3% of the $REO_{1.5}$ constituents, and over 97% of the $REO_{1.5}$ constituents is $YbO_{1.5}$. It is reasonable to speculate that the collected minor Sc signals in apatite are due to the insufficient precision of EDS. The crystallization of apatite is induced by the $YbO_{1.5}$ constituent in solid solution, and the $ScO_{1.5}$ constituent is not involved in the reaction. Therefore, the decreased $YbO_{1.5}$ content in $(Sc_xYb_{1-x})O_{1.5}$ solid solutions causes a slight reduction of $REO_{1.5}$ content in apatite, and even the disappearance of apatite grains.

Table 3. Measured apatite compositions in treated mixtures with $REO_{1.5}$:CMAS ratios of 1:10 and 1:5.

Mixtures	**Chemical composition (mol%, EDS)**				
	CaO	**SiO_2**	**$ScO_{1.5}$**	**$YbO_{1.5}$**	**$REO_{1.5}$**
$YbO_{1.5}$:CMAS = 1:10	15.7 ± 0.5	37.1 ± 0.2	—	47.2 ± 0.2	47.2
$YbO_{1.5}$:CMAS = 1:5	16.0 ± 1.2	36.6 ± 1.2	—	47.4 ± 2.4	47.4
$(Sc_{0.1}Yb_{0.9})O_{1.5}$:CMAS = 1:10	16.7 ± 0.3	39.1 ± 0.1	1.0 ± 0.2	43.2 ± 0.1	44.2
$(Sc_{0.1}Yb_{0.9})O_{1.5}$:CMAS = 1:5	18.5 ± 0.8	42.8 ± 0.9	0.6 ± 0.1	38.1 ± 0.4	38.7
$(Sc_{0.2}Yb_{0.8})O_{1.5}$:CMAS = 1:5	18.9 ± 0.3	41.8 ± 0.4	1.0 ± 0.1	38.2 ± 0.1	39.2
$(Sc_{0.3}Yb_{0.7})O_{1.5}$:CMAS = 1:5	18.0 ± 0.1	38.9 ± 0.1	1.2 ± 0.1	41.9 ± 0.1	43.1

The crystallization of silicocarnotite requires a high $REO_{1.5}$ content in the mixtures,

and Table 4 summarizes the measured compositions. The silicocarnotite phase contains the same constituents as apatite, i.e., CaO, SiO_2 and $REO_{1.5}$, while the appearance of silicocarnotite is attributed to the variation of the Ca:Si ratio in CMAS melt during the corrosion reaction process, which has been discussed in our previous work[17]. Silicocarnotite products with similar compositions have been observed in the reaction of gadolinium oxide[28], yttrium oxide[18, 28], yttrium zirconate[28] or ytterbium hafnate[29] with CMAS deposits. The $REO_{1.5}$ content in silicocarnotite is in a range of 25 ~ 27 mol%, which is much lower than that in apatite. Moreover, the $ScO_{1.5}$ content is less than 2 mol%, which indicates that the formation of silicocarnotite is less dependent on the $ScO_{1.5}$ constituent.

Table 4. Measured silicocarnotite compositions in treated mixtures with a $REO_{1.5}$:CMAS ratio of 1:5.

Mixtures	**Chemical composition (mol%, EDS)**				
	CaO	**SiO_2**	**$ScO_{1.5}$**	**$YbO_{1.5}$**	**$REO_{1.5}$**
$YbO_{1.5}$:CMAS = 1:5	35.2 ± 0.4	39.7 ± 0.4	—	25.1 ± 0.6	25.1
$(Sc_{0.1}Yb_{0.9})O_{1.5}$:CMAS = 1:5	36.0 ± 0.6	39.1 ± 0.6	0.9 ± 0.4	23.9 ± 0.3	24.8
$(Sc_{0.2}Yb_{0.8})O_{1.5}$:CMAS = 1:5	36.6 ± 0.8	36.8 ± 1.8	1.6 ± 0.1	25.0 ± 1.0	26.6
$(Sc_{0.3}Yb_{0.7})O_{1.5}$:CMAS = 1:5	36.7 ± 0.4	36.2 ± 0.1	1.0 ± 0.1	26.1 ± 0.3	27.1

The garnet precipitates, which effectively solidify the CMAS melt, crystallizes in almost all the mixtures, as illustrated in Figure 2. The measured garnet compositions are summarized in Table S2. It is found that garnet contains all constituents in $(Sc_xYb_{1-x})O_{1.5}$-CMAS system and its composition exhibits a strong dependence on the composition of $(Sc_xYb_{1-x})O_{1.5}$ solid solutions, which is distinct from the two crystalline products discussed previously. Figure 3 depicts the variation of CaO, $YbO_{1.5}$, $ScO_{1.5}$,

MgO, $AlO_{1.5}$ and SiO_2 constituents in garnet with the composition of $(Sc_xYb_{1-x})O_{1.5}$ solid solutions. The $YbO_{1.5}$ and $ScO_{1.5}$ concentration in garnet exhibits a coincident tendency as those in solid solution. The $YbO_{1.5}$ content in garnet decreases from 16.2 and 23.0 mol% to 0 mol% (Figure 3a and 3b), while the $ScO_{1.5}$ content increases from 0 mol% to 24.6 and 27.0 mol% (Figure 3c and 3d). It inevitably leads to coupling variations in the other constituents, which is an increase of CaO content and a decrease in MgO and $AlO_{1.5}$ content. The compensation variations are further confirmed by the small fluctuations in the contents of CaO + $YbO_{1.5}$ and $ScO_{1.5}$ + MgO + $AlO_{1.5}$, which maintain in the range of 35 ~ 40 mol% (Figure 3a and 3b) and 24 ~ 30 mol% (Figure 3c and 3d), respectively. The coupling variation of $ScO_{1.5}$, MgO and $AlO_{1.5}$ suggests their similar contribution in forming garnet, as expected. The SiO_2 content is negligibly affected by the composition of $(Sc_xYb_{1-x})O_{1.5}$ solid solutions and maintains 31 ~ 37 mol% (Figure 3e and 3f). It is reasonably speculated that constituent concentration in garnet is dominant by its special crystal structure, which will be discussed in detail subsequently.

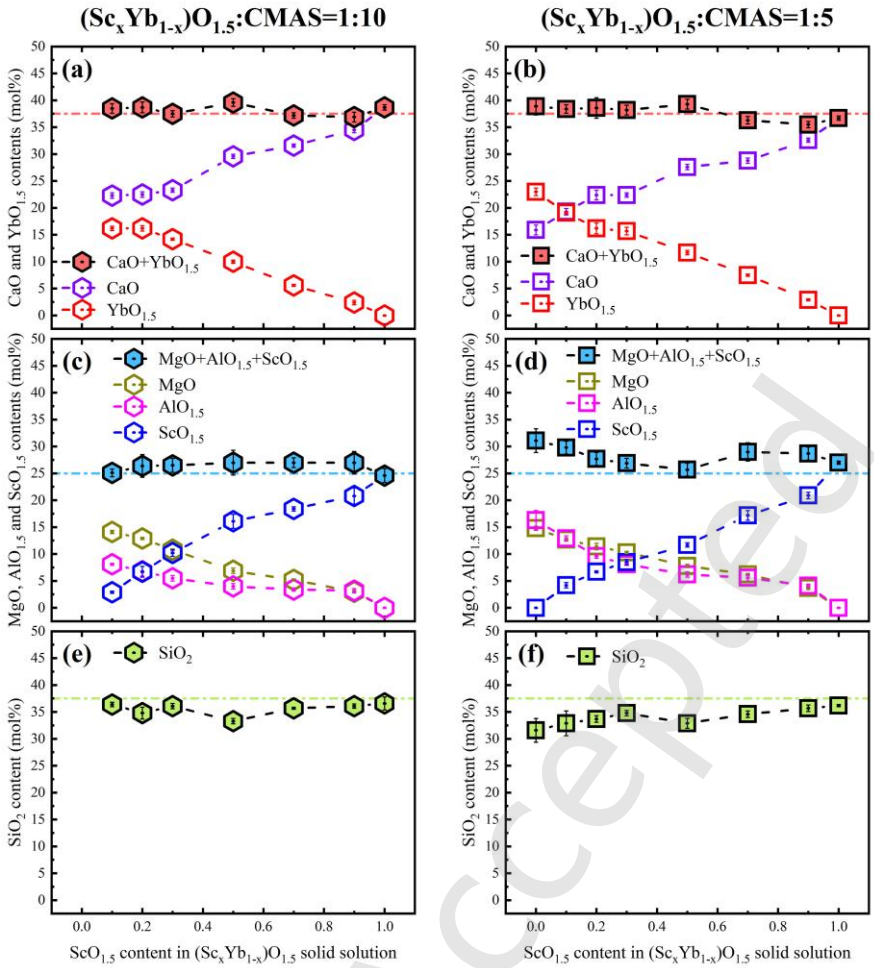

Figure 3. The variation of CaO, $YbO_{1.5}$, $ScO_{1.5}$, MgO, $AlO_{1.5}$ and SiO_2 constituents in garnet with the $ScO_{1.5}$ content in $(Sc_xYb_{1-x})O_{1.5}$ solid solution.

The diopside phase is observed in the interaction between CMAS deposits and solid solutions with $ScO_{1.5}$ content exceeding 70 mol%. At present, there are few reports on diopside as a CMAS corrosion product. Table 5 shows the measured composition. Diopside contains all constituents involved in $(Sc_xYb_{1-x})O_{1.5}$-CMAS system. In contrast to other three crystalline products, diopside contains the lowest $REO_{1.5}$ content, i.e., 11 ~ 13 mol%, which indicates its merits in melt consumption. It should be noticed that the $YbO_{1.5}$ content in diopside is less than 1 mol%. Diopside is almost free of ytterbium constituent and its crystallization is induced by the $ScO_{1.5}$ constituent.

Table 5. Measured diopside compositions in treated mixtures with $REO_{1.5}$:CMAS ratios of 1:10 and 1:5.

Mixtures	Chemical composition (mol%, EDS)						
	CaO	MgO	$AlO_{1.5}$	SiO_2	$ScO_{1.5}$	$YbO_{1.5}$	$REO_{1.5}$
$(Sc_{0.7}Yb_{0.3})O_{1.5}$:CMAS = 1:5	25.3 ± 0.2	11.8 ± 0.3	14.4 ± 0.5	36.8 ± 0.4	10.6 ± 0.2	1.0 ± 0.1	11.6
$(Sc_{0.9}Yb_{0.1})O_{1.5}$:CMAS = 1:10	25.4 ± 0.9	11.9 ± 0.8	13.4 ± 0.3	39.5 ± 0.6	9.6 ± 1.0	0.2 ± 0.1	12.1
$(Sc_{0.9}Yb_{0.1})O_{1.5}$:CMAS = 1:5	24.7 ±0.3	10.0 ± 0.3	14.6 ± 0.3	38.6 ± 0.8	11.4 ± 0.9	0.6 ± 0.1	12.0
$ScO_{1.5}$:CMAS = 1:10	26.3 ± 1.0	11.1 ± 0.8	12.9 ± 0.4	38.2 ± 0.6	11.5 ± 0.6	—	11.5

4. Discussion

4.1 Implication of crystalline products on CMAS corrosion behavior

At high temperatures, the eutectic reaction melts the CMAS deposit into a liquid[15, 18], which accelerates dissolution of the coating or material constituents. Once reaching the threshold, these constituents separate from the melt and crystallize into various products. Crystallization behaviors are divided into three categories[28]: intrinsic crystallization, reprecipitation and reactive crystallization. The intrinsic crystallization products, such as calcium silicate, gehlenite, spinel, etc.[6, 28], mostly appear during cooling and merely contain constituents from CMAS deposits. The reprecipitation generates crystalline products with an identical or slightly modified composition of coating constituents. The intrinsic crystallization and reprecipitation have little or even no effect on the corrosion behavior. The reactive crystallization involves the consumption of both coating and deposits, which could be the basis for mitigation strategies of CMAS. In the $(Sc_xYb_{1-x})O_{1.5}$-CMAS system, apatite, silicocarnotite, garnet and diopside have been demonstrated as reactive crystallization

products.

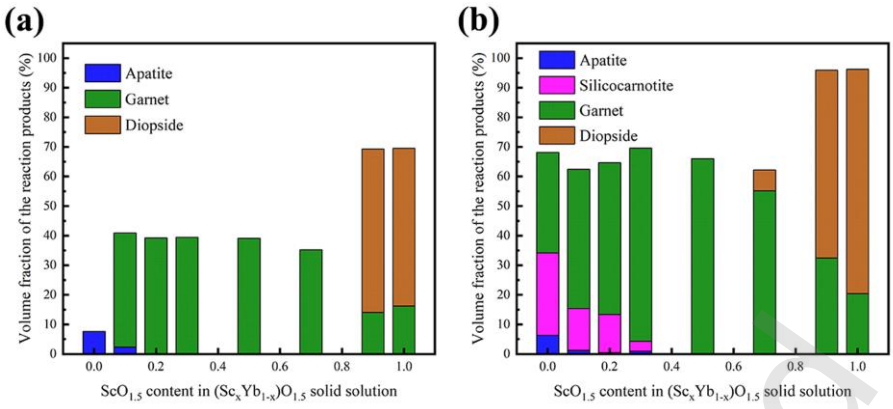

Figure 4. Volume fraction of reaction products in treated mixtures with $REO_{1.5}$:CMAS ratios of (a) 1:10 and (b) 1:5.

The ability to melt consumption is represented by the volume fraction of reactive crystallization products. The volume fraction is directly calculated according to quantitative metallography[30], which utilizes the principles of statistical and stochastic geometry in stereology to relate three-dimensional (3D) microstructure characteristics to the data measured on the two-dimensional (2D) metallographic sections. Figure 4a shows the volume fraction of reaction products in samples with a $REO_{1.5}$:CMAS ratio of 1:10, calculated according to the corresponding area fraction in BSD images (Figure 2a-h). The reaction products involve apatite, garnet and diopside. In the absence of $ScO_{1.5}$ constituent, apatite crystallizes, with the volume fraction less than 10 vol%. When the $ScO_{1.5}$ content appears in solid solution, the reaction product is converted into garnet-dominant, with ~ 40 vol% of crystallization in the sample. For $(Sc_{0.9}Yb_{0.1})O_{1.5}$ and $ScO_{1.5}$, diopside becomes the main product together with garnet, which promotes further crystallization with the volume fraction of 70%. The dramatic increase in the volume fraction of reaction products demonstrates the influence of Sc^{3+}

on crystallization behavior of Yb-based coatings against CMAS deposits.

The volume fraction of crystalline products in mixtures with a $REO_{1.5}$:CMAS ratio of 1:5 is much higher than that with the ratio of 1:10, as shown in Figure 4b. In the sample absent of $ScO_{1.5}$ constituent, besides a small amount of apatite, garnet and silicocarnotite have crystallized, and the volume fraction of three reaction products reaches to 68%. The increased $ScO_{1.5}$ content in $(Sc_xYb_{1-x})O_{1.5}$ solid solutions result in garnet becoming the dominant crystalline product. For $(Sc_{0.9}Yb_{0.1})O_{1.5}$ and $ScO_{1.5}$, massive precipitated diopside with the volume fraction of reaction products to 90% was observed.

According to the measured compositions (Table 3, 5 and S2), the $REO_{1.5}$ content in garnet and silicocarnotite or diopside is half or a quarter of that in apatite. In terms of the ability to consume melt, the following sequence is proposed: diopside > garnet ≈ silicocarnotite > apatite. Diopside is extremely effective in solidifying the CMAS melt, but its formation requires an excessive amount of scandium constituent. Therefore, the optimization of CMAS-resistant EBCs is expected to focus on transforming from apatite to garnet by means of introducing scandium constituent. Scandium together with yttrium or lanthanides has been demonstrated to form silicate solid solutions[31, 32], which suggests its compatibility with current EBC systems.

4.2 Correlation on cation partitioning in reactive crystallization products

In previous sections, the scandium-ytterbium oxide solid solution has been found to efficiently facilitate the precipitation of garnet and diopside. It is hypothesized that the scandium and ytterbium constituents play different roles during the reactive

crystallization, and detailed discussions on the crystal structures of four crystalline products and the site occupancy of cations are conducted.

Apatite exhibits a hexagonal structure with space group *P6₃/m* and its stoichiometry is expressed as $A^{□}_4A^{□}_6T_6O_{26}$ in which '$A^{□}$', '$A^{□}$', and 'T' represent crystallographic cationic sites. The crystal structure of apatite has been extensively investigated[33, 34], by means of time-of-flight neutron diffraction together with the Rietveld method[35]. Based on that information as well as the quantitative results in section 3.2.2, the cation assignments in this work have been depicted and illustrated in Figure 5a. Si^{4+} occupies the T site and forms the [SiO_4] tetrahedron with oxygen anions, while the dimension of corresponding internal space formed by oxygen anions determines that the $A^{□}$ site tends to be occupied by Yb^{3+} and the 9-coordinate $A^{□}$ site accommodates both Ca^{2+} and Yb^{3+}. The almost negligible $ScO_{1.5}$ content implies that apatite cannot accommodate Sc^{3+}. With a variation of Ca:Yb ratio at the $A^{□}$ site, oxygen vacancies form in the apatite structure for charge balance. The unique crystal structure allows the composition of apatite, which crystallizes as a CMAS corrosion product, to vary within a given range, from defect-free $Ca_2RE_8(SiO_4)_6O_2$ to oxygen-vacancy-containing $Ca_4RE_6(SiO_4)_6O$.

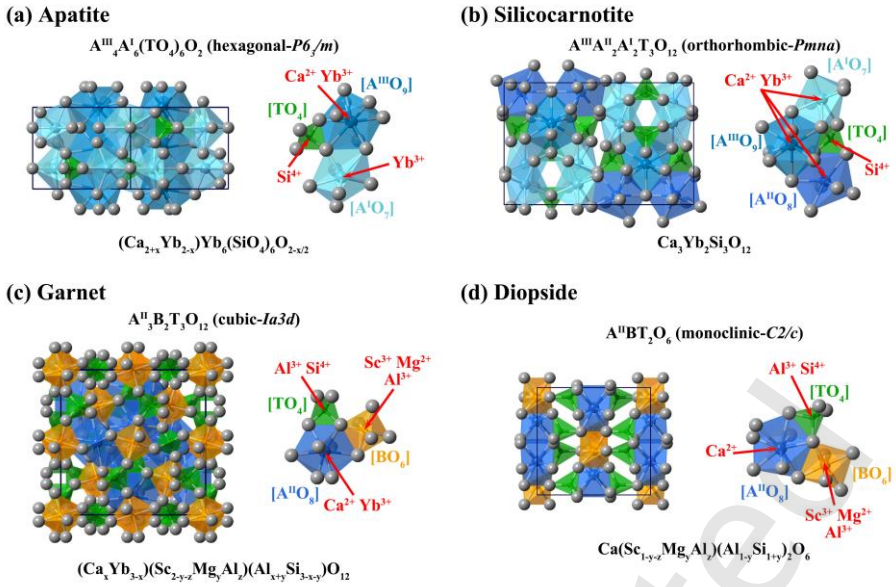

Figure 5. Schematic diagram of crystal structure and cation occupancy in (a) apatite, (b) silicocarnotite, (c) garnet and (d) diopside.

Silicocarnotite belongs to the orthorhombic system with space group *Pmna*, which is represented as $A^{\square}A^{\square}_2A^{\square}_2T_3O_{12}$. Based on the structural formula of $(Ca_{0.84}Y_{0.16})$-$(Ca_{0.41}Y_{0.59})_2(Ca_{0.67}Y_{0.33})_2(SiO_4)_3$ refined by Yamane et. al[36], it is reasonably concluded that Ca^{2+} and Yb^{3+} non-equivalently co-occupy the 7-coordinate $A^{\square}$ site, 8-coordinate $A^{\square}$ site and 9-coordinate $A^{\square}$ site in silicocarnotite precipitates, while Si^{4+} occupies the 4-coordinate T sites. The schematic diagram of corresponding crystal structure is shown in Figure 5b. The measured silicocarnotite compositions in the different samples matches well with the stoichiometry, $Ca_3Yb_2Si_3O_{12}$, in accordance with other investigations[18, 28].

The garnet phase with cubic structure (*I*a3d) can be expressed as $A^{\square}_3B_2T_3O_{12}$, in which '$A^{\square}$', 'B' and 'T' represent 8-, 6- and 4-coordinate crystallographic cationic sites[22]. Godbole et al.[10, 11] has reported the cation assignments for garnet structure in Al-Ca-Mg-Si-(Gd/Y/Yb)-O systems based on Pauling's rules. Based on relevant

research on the crystal chemistry of garnet[22], it is known that Sc^{3+} and Mg^{2+} with similar sizes can be distributed in an identical crystallographic site. As shown in Figure 5c, Ca^{2+} and Yb^{3+} occupy the A□ site, Sc^{3+} together with Mg^{2+} and Al^{3+} occupies the B site, and the T site accommodates Si^{4+} and partial Al^{3+}. Large-size cations are introduced into the high-coordinate sites, and small-size ones preferentially accommodate in the low-coordinate ones, which effectively reduces the aberrations in the crystal structure with improved stability. According to the literatures[10, 11, 22], vacancies or interstitial defects are not required in garnet, because the nonequivalent cationic substitutions in garnet tend to be coupled maintaining the total cation charge. It is evident from the composition variations of Figure 3 that the substitution of Yb^{3+} by Ca^{2+} in A□ site is coupled with the substitution of Mg^{2+} by Sc^{3+} in B site and/or Si^{4+} by Al^{3+} in T site. These coupled substitutions result in the $REO_{1.5}$ content with the range of 19 ~ 26 mol% in garnet. The diffraction peak of garnet systematically shifted towards the low-angle region (in Figure 2), which indicates an increase of the lattice constants. More importantly, the melt composition varies with the Sc:Yb ratio in solid solutions and precipitation of garnet, which has great influence on the mitigation of CMAS corrosion.

The A□BT_2O_6 diopside exhibits a monoclinic structure (*C2/c*), and also contains 8, 6 and 4-fold coordinated cation sublattices[37]. Based on the arrangement of relevant oxygen anions and the dimension of resultant internal spaces, Sc^{3+}, Ca^{3+}, Mg^{2+}, Al^{3+}, and Si^{4+} are assigned in diopside structure, as depicted in Figure 5d. The cation partitioning results are similar to those of garnet, which is in accordance with other

investigations on diopside[37, 38]. However, the large internal space in [A□O_8] polyhedron of diopside may be inappropriate to the introduction of Yb^{3+}, so Yb^{3+} is hardly detected in diopside grains.

In $(Sc_xYb_{1-x})O_{1.5}$-CMAS systems, Yb^{3+} and Sc^{3+} occupy different crystallographic sites in reactive crystallization products. Similar to Ca^{2+}, Yb^{3+} tends to form high-coordination polyhedrons, [$AO_{7/8/9}$], and Sc^{3+} exhibits a similar behavior as Mg^{2+} and Al^{3+}, promoting the formation of [BO_6] coordination polyhedrons. In terms of crystal structure characteristics, the dominant difference among apatite/silicocarnotite and garnet/diopside is the [BO_6] coordination polyhedron. In the absence of $ScO_{1.5}$ constituent, the [Ca/$YbO_{7/8/9}$] polyhedrons and [SiO_4] tetrahedrons preferentially crystallize into apatite and silicocarnotite. The [ScO_6] polyhedrons substitute the [Mg/AlO_6] polyhedrons to promote the formation of garnet or diopside.

4.3 Pseudo-ternary phase diagram in EBC-CMAS systems

CMAS corrosion is inevitable for EBCs. The diversity of coating-deposit system poses a significant challenge to the prediction or evaluation of reactive crystallization behavior. The phase equilibrium in coating-deposit systems have shown the merits for coating design[39, 40]. In the previous discussion, it is found that the cations from coatings and deposits have commonality in site occupancy of several crystallization products. In this section, it is focused on reclassifying the complicated constituents in the $REO_{1.5}$-CMAS system and developing a pseudo-ternary phase diagram to predict the crystalline products in various coating-deposit systems.

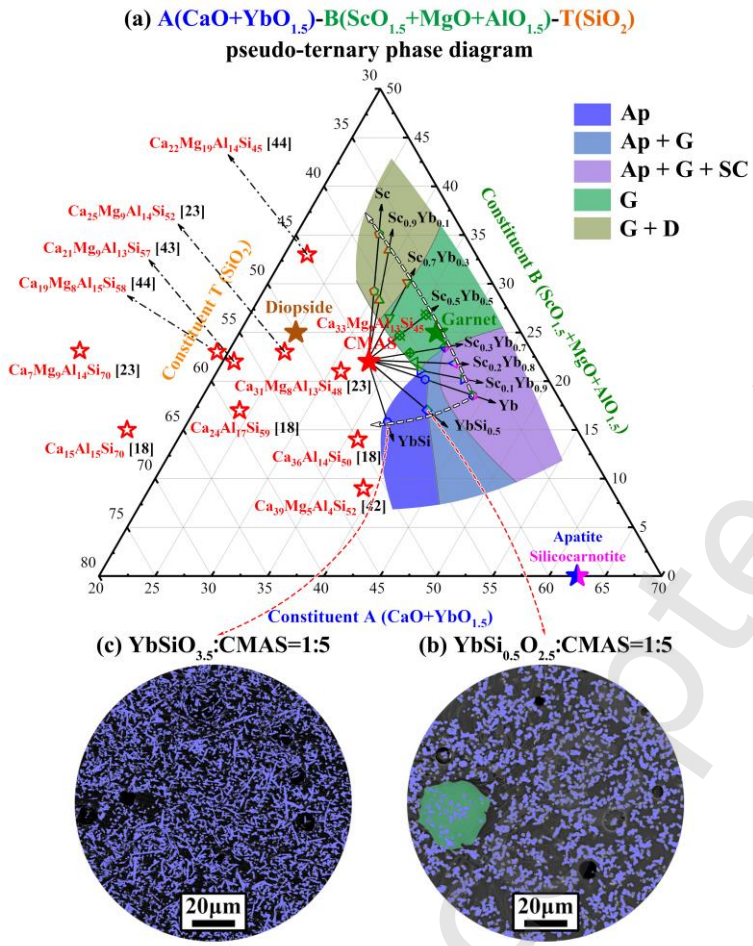

Figure 6. (a) A-B-T pseudo-ternary phase diagrams in $(Sc_xYb_{1-x})O_{1.5}$-CMAS system; (b and c) BSE micrographs of $YbSi_{0.5}O_{2.5}$/ $YbSiO_{3.5}$-CMAS mixtures treated at 1300 ^oC for 1 h

The constituents in $(Sc_xYb_{1-x})O_{1.5}$-CMAS systems are normalized and divided into three groups: 'A' ($CaO+YbO_{1.5}$), 'B' ($ScO_{1.5}+MgO+AlO_{1.5}$) and 'T' (SiO_2), based on the commonality of cationic partitioning. The $(Sc_xYb_{1-x})O_{1.5}$-CMAS mixtures with various compositions are expressed as points in A-B-T system, as shown in Table S3. The converted compositions are marked by hollow polygons and filled with corresponding colors in Figure 6a, according to the phase composition of reaction products. The CMAS deposit and reactive crystallization products are also projected

into the A-B-T system, which are represented by solid pentagrams with different colors. Several equilibrium fields, 'Ap + G + SC', 'G' and 'G + D', are initially delineated by the connection of hollow polygons with the same phase combination. The A-B-T pseudo-ternary phase diagram visualizes the relationship between the crystalline products and the composition of coating-deposit systems. For the selected $Ca_{33}Mg_9Al_{13}Si_{45}$, the incorporation of $(Sc_xYb_{1-x})O_{1.5}$ solid solutions leads to the evolution of system composition towards different directions, as illustrated by black arrows in Figure 6a. The increased $ScO_{1.5}$ content in solid solutions results in a counterclockwise rotation of the black arrows. The terminal composition of the coating-deposit system proceeds from the 'Ap + G + SC' region, traverses through the 'G' region and eventually reaches the 'G + D' region.

To further validate the established relationship, two widely investigated EBC materials, ytterbium monosilicate and disilicate, are blended with CMAS powders in a ratio of 1:5 and heat-treated at 1300ºC. Figure 6b and 6c illustrate their microstructure. The dominant reaction product of CMAS deposit with two ytterbium silicates is apatite, and garnet merely crystallizes in small quantities in the ytterbium monosilicate sample. Zhao et al.[41] demonstrated that merely apatite was observed as reactive crystallization product during the CMAS corrosion of ytterbium disilicate APS coatings. Liu et al.[13] reported the crystallization of apatite and garnet in the interaction of ytterbium monosilicate APS coatings with CMAS melt. The thermodynamic investigation of ytterbium silicates and CMAS deposits is consistent with the reported CMAS corrosion behavior of relevant coatings. These two mixtures are also converted

correspondingly in the phase diagram, and marked by a hollow circle and rhombus, respectively. The incorporation of SiO_2 constituent in coating materials compel the black arrows which represent the evolution of system composition to rotate clockwise. Therefore, the terminal composition of the coating-deposit system moves away from 'Ap + G + SC' and 'G' regions, and garnet gradually decreases or even disappears. The results are in accordance with the expectation of established phase diagram. The supplementary experiments on rare-earth silicates contribute to the further delineation of two equilibrium phase regions: 'Ap' and 'Ap + G'. It is worth noting that silicocarnotite also disappears with the incorporation of SiO_2 into coating materials. The established phase diagram exhibits limitations in accurately depicting competition between apatite and silicocarnotite, because the constituent grouping forces apatite and silicocarnotite to be projected to the same point.

In actual service environments, deposits are derived from different siliceous minerals, which leads to the diversity in their chemical composition[6, 39]. The deposits reported in relevant investigations include: $Ca_{36}Al_{14}Si_{50}$, $Ca_{24}Al_{17}Si_{59}$, $Ca_{15}Al_{15}Si_{70}$, $Ca_{31}Mg_8Al_{13}Si_{48}$, $Ca_{25}Mg_9Al_{14}Si_{52}$, $Ca_7Mg_9Al_{14}Si_{70}$, $Ca_{39}Mg_5Al_4Si_{52}$, $Ca_{21}Mg_9Al_{13}Si_{57}$, $Ca_{22}Mg_{19}Al_{14}Si_{45}$, $Ca_{19}Mg_8Al_{15}Si_{58}$, etc.[18, 23, 42-44]. These deposits are also projected in the established phase diagram, and marked by hollow pentagrams, as shown in Figure 6a. In comparison with $Ca_{33}Mg_9Al_{13}Si_{45}$, the hollow pentagrams representing these deposits move to the left region in the phase diagram, away from 'Ap + G + SC' and 'G' regions. The reactive crystallization products between these deposits and Yb-based coatings/materials are apatite dominant [23, 43, 44]. Based on

the established phase diagram, it can be deduced that the introduction of the $ScO_{1.5}$ constituent is indispensable to achieve garnet crystallization in these coating-deposit systems. Given the complexity of the deposit composition and the diversity of optional coating materials, the developed A-B-T pseudo-ternary phase diagram has a wide prospect for targeted design of coatings to improve the corrosion resistance. However, the established phase diagram still has inadequacies, and therefore relevant efforts for its improvement and optimization are indispensable.

5. Conclusion

The phase equilibrium in the $(Sc_xYb_{1-x})O_{1.5}$-CMAS system at 1300 °C was investigated by heat treatment of mixtures. The conclusions include:

a. The rection products between scandium-ytterbium oxide solid solutions with the CMAS deposit include apatite, silicocarnotite, garnet and diopside. The substitution of $ScO_{1.5}$ content leads to the transformation of reaction products from apatite/silicocarnotite to garnet and then diopside, which effectively consumes the melt. It is expected to prevent the melt infiltration and maintain the coating validity.

b. Sc^{3+} demonstrates differently from Yb^{3+} in the formation of crystalline products: Yb^{3+} tends to occupy high-coordinate (7, 8 and 9-coordinate) sites in the crystal structure, while Sc^{3+} forms $[BO_6]$ coordination polyhedron with oxygen anions, thus promoting the crystallization of garnet and diopside.

c. Based on the commonality of cation occupancy in crystallography, an A-B-T pseudo-ternary phase diagram is established to describe the phase equilibrium

in coating-deposit systems, which is expected to predict corrosion behavior and design of corrosion resistant coating materials.

Supplementary information

Supplementary material related to this article can be found online.

Acknowledgments

This work was supported by the National Natural Science Foundation of China under Grant Nos. U21A2063, 52372071, 52002376, 52302076; National Key R&D Program of China under Grant No. 2021YFB3702300; Liaoning Revitalization Talents Program under Grant No. XLYC2002018; International Partnership Program of the Chinese Academy of Sciences under Grant No. 172GJHZ2022094FN.

References

[1] Song C, Ye F, Cheng L*, et al.* Long-term ceramic matrix composite for aeroengine. *J Adv Ceram* 2022, **11**: 1343-1374.

[2] Tejero-Martin D, Bennett C, Hussain T. A review on environmental barrier coatings: History, current state of the art and future developments. *J Eur Ceram Soc* 2021, **41**: 1747-1768.

[3] Nieto A, Agrawal R, Bravo L*, et al.* Calcia-magnesia-alumina-silicate (CMAS) attack mechanisms and roadmap towards sandphobic thermal and environmental barrier coatings. *Int Mater Rev* 2020: 1-42.

[4] Levi CG, Hutchinson JW, Vidal-Sétif M-H*, et al.* Environmental degradation of thermal-barrier coatings by molten deposits. *MRS Bull* 2012, **37**: 932-941.

[5] Paksoy AH, Xiao P. Review of processing and design methodologies of environmental barrier coatings for next generation gas turbine applications. *Adv Appl Ceram* 2023, **122**: 36-56.

[6] Poerschke DL, Jackson RW, Levi CG. Silicate deposit degradation of engineered coatings in gas turbines: progress toward models and materials solutions. *Annu Rev Mater Res* 2017, **47**: 297-330.

[7] Chen X, He MY, Spitsberg I*, et al.* Mechanisms governing the high temperature erosion of thermal barrier coatings. *Wear* 2004, **256**: 735-746.

[8] Chen X. Calcium-magnesium-alumina-silicate (CMAS) delamination mechanisms in EB-PVD thermal barrier coatings. *Surf Coat Tech* 2006, **200**: 3418-3427.

[9] Mercer C, Faulhaber S, Evans AG*, et al.* A delamination mechanism for thermal

barrier coatings subject to calcium-magnesium-alumino-silicate (CMAS) infiltration. *Acta Mater* 2005, **53**: 1029-1039.

[10] Godbole E, Karthikeyan N, Poerschke D. Garnet stability in the Al-Ca-Mg-Si-Y-O system with implications for reactions between TBCs, EBCs, and silicate deposits. *J Am Ceram Soc* 2020, **103**: 5270-5282.

[11] Godbole E, von der Handt A, Poerschke D. Apatite and garnet stability in the Al-Ca-Mg-Si-(Gd/Y/Yb)-O systems and implications for T/EBC: CMAS reactions. *J Am Ceram Soc* 2021, **105**: 1596-1609.

[12] Zhong X, Wang Y, Liu P*, et al.* Effects of microstructure on corrosion behaviors for RE_2SiO_5 (RE=Gd, Y, Er) environmental barrier coatings against calcium-magnesium-alumino-silicate melts. *Corros Sci* 2022, **199**: 110174.

[13] Liu P, Zhong X, Niu Y*, et al.* Reaction behaviors and mechanisms of tri-layer $Yb_2SiO_5/Yb_2Si_2O_7$/Si environmental barrier coatings with molten calcium-magnesium-alumino-silicate. *Corros Sci* 2022, **197**: 110069.

[14] Poerschke DL, Hass DD, Eustis S*, et al.* Stability and CMAS resistance of ytterbium-silicate/hafnate EBCs/TBC for SiC composites. *J Am Ceram Soc* 2015, **98**: 278-286.

[15] Song W, Lavallee Y, Hess KU*, et al.* Volcanic ash melting under conditions relevant to ash turbine interactions. *Nat Commun* 2016, **7**: 10795.

[16] Webster RI, Opila EJ. Viscosity of CaO-MgO-Al_2O_3-SiO_2 (CMAS) melts: Experimental measurements and comparison to model calculations. *J Non-cryst Solids* 2022, **584**: 121508.

[17] Zhang G, Zhang J, Wang J. Synthesis and characterization of ytterbium oxide: A novel CMAS-resistant environmental barrier coating material. *J Am Ceram Soc* 2022, **106**: 621-631.

[18] Poerschke DL, Barth TL, Levi CG. Equilibrium relationships between thermal barrier oxides and silicate melts. *Acta Mater* 2016, **120**: 302-314.

[19] Opila EJ. Thermodynamics and kinetics of gaseous metal hydroxide formation from oxides relevant to power and propulsion applications. *Calphad* 2016, **55**: 32-40.

[20] Kolitsch U, Seifert HJ, Ludwig T*, et al.* Phase equilibria and crystal chemistry in the Y_2O_3-Al_2O_3-SiO_2 system. *J Mater Res* 1999, **14**: 447-455.

[21] Shannon RD. Revised effective ionic radii and systematic studies of interatomic distances in halides and chalcogenides. *Acta Crystallogr A* 1976, **32**: 751-767.

[22] Novak GA, Gibbs GV. The crystal chemistry of the silicate garnets. *Am Mineral* 1971, **56**: 791-825.

[23] Stokes JL, Harder BJ, Wiesner VL*, et al.* High-Temperature thermochemical interactions of molten silicates with $Yb_2Si_2O_7$ and $Y_2Si_2O_7$ environmental barrier coating materials. *J Eur Ceram Soc* 2019, **39**: 5059-5067.

[24] Abdul-Jabbar NM, Poerschke DL, Gabbett C*, et al.* Phase equilibria in the zirconia-yttria/gadolinia-silica systems. *J Eur Ceram Soc* 2018, **38**: 3286-3296.

[25] Perrudin F, Vidal-Sétif MH, Rio C*, et al.* Influence of rare earth oxides on kinetics and reaction mechanisms in CMAS silicate melts. *J Eur Ceram Soc* 2019, **39**: 4223-4232.

[26] Perrudin F, Rio C, Vidal-Sétif MH*, et al.* Gadolinium oxide solubility in molten

silicate: dissolution mechanism and stability of $Ca_2Gd_8(SiO_4)_6O_2$ and $Ca_3Gd_2(Si_3O_9)_2$ silicate phases. *J Eur Ceram Soc* 2017, **37**: 2657-2665.

[27] Borom MP, Johnson CA, Peluso LA. Role of environmental deposits and operating surface temperature in spallation of air plasma sprayed thermal barrier coatings. *Surf Coat Tech* 1996, **86**: 116-126.

[28] Poerschke DL. Developments in thermodynamic models of deposit-induced corrosion of high-temperature coatings. *JOM* 2021, **74**: 260-273.

[29] Poerschke DL, Seward GGE, Levi CG*, et al.* Influence of Yb:Hf ratio on ytterbium hafnate/molten silicate (CMAS) reactivity. *J Am Ceram Soc* 2016, **99**: 651-659.

[30] Gokhale AM. Utility of stereology for quantitative metallography. Symposium on Commemorating 100 Years of E04 Development of Metallographic Standards.Astm International. Atlanta, GA: Astm International; 2017. p. 37-52.

[31] Escudero A, Alba MD, Becerro AI. Polymorphism in the $Sc_2Si_2O_7$-$Y_2Si_2O_7$ system. *J Solid State Chem* 2007, **180**: 1436-1445.

[32] Wang X, He Y, Wang C*, et al.* Thermal performance regulation of high-entropy rare-earth disilicate for thermal environmental barrier coating materials. *J Am Ceram Soc* 2022, **105**: 4588-4594.

[33] Poerschke DL, Barth TL, Fabrichnaya O*, et al.* Phase equilibria and crystal chemistry in the calcia-silica-yttria system. *J Eur Ceram Soc* 2016, **36**: 1743-1754.

[34] White TJ, ZhiLi D. Structural derivation and crystal chemistry of apatites. *Acta Crystallogr B* 2003, **59**: 1-16.

[35] Fahey JA, Wwber WJ, Rotella aFJ. An X-ray and neutron powder diffraction study

of the $Ca_{2+x}Nd_{8-x}(SiO_4)_6O_{2-0.5x}$ system. *J Solid State Chem* 1985, **60**: 145-158.

[36] Yamane H, Nagasawa T, Shimada M*, et al.* $Ca_3Y_2(SiO_4)_3$. *Acta Crystallogr C* 1997, **53**: 1367-1369.

[37] Haruo O, Nobuo L. Structure of $CaScAlSiO_6$-pyroxene. *J Jpn Assoc Mineral Petrol Econ Geol* 1978: 267-273.

[38] Tribaudino M. High-temperature crystal chemistry of C2/c clinopyroxenes along the join $CaMgSi_2O_6$-$CaAl_2SiO_6$. *Eur J Mineral* 1996, **8**: 273-279.

[39] Ericks AR, Zok FW, Poerschke DL*, et al.* Protocol for selecting exemplary silicate deposit compositions for evaluating thermal and environmental barrier coatings. *J Am Ceram Soc* 2022, **105**: 3665-3688.

[40] Summers WD, Poerschke DL, Begley MR*, et al.* A computational modeling framework for reaction and failure of environmental barrier coatings under silicate deposits. *J Am Ceram Soc* 2020, **103**: 5196-5213.

[41] Zhao H, Richards BT, Levi CG*, et al.* Molten silicate reactions with plasma sprayed ytterbium silicate coatings. *Surf Coat Tech* 2016, **288**: 151-162.

[42] Drexler JM, Aygun A, Li D*, et al.* Thermal-gradient testing of thermal barrier coatings under simultaneous attack by molten glassy deposits and its mitigation. *Surf Coat Tech* 2010, **204**: 2683-2688.

[43] Webster RI, Opila EJ. Mixed phase ytterbium silicate environmental-barrier coating materials for improved calcium-magnesium-alumino-silicate resistance. *J Mater Res* 2020, **35**: 2358-2372.

[44] Wu Y, Zhi W, Li Y*, et al.* Interactions between rare-earth zirconates ($RE_2Zr_2O_7$)

and CMAS silicate melts. *Corros Sci* 2023, **224**: 111526.

Table captions

Table 1. Chemical compositions of apatite phase in CMAS corrosion of several coatings or materials

Table 2. Chemical compositions of garnet phase in CMAS corrosion of several coatings or materials

Table 3. Measured apatite compositions in treated mixtures with $REO_{1.5}$:CMAS ratios of 1:10 and 1:5.

Table 4. Measured silicocarnotite compositions in treated mixtures with a $REO_{1.5}$:CMAS ratio of 1:5.

Table 5. Measured diopside compositions in treated mixtures with $REO_{1.5}$:CMAS ratios of 1:10 and 1:5.

Figure captions

Figure 1. XRD patterns and EDS mapping of $(Sc_xYb_{1-x})O_{1.5}$ solid-solution powders with various compositions: x = 0.0, 0.1, 0.2, 0.3, 0.5, 0.7, 0.9 and 1.0, from top to bottom.

Figure 2. XRD patterns and BSE micrographs of $(Sc_xYb_{1-x})O_{1.5}$-CMAS mixtures treated at 1300 ºC for 1 h.

Figure 3. The variation of CaO, $YbO_{1.5}$, $ScO_{1.5}$, MgO, $AlO_{1.5}$ and SiO_2 constituents in garnet with the $ScO_{1.5}$ content in $(Sc_xYb_{1-x})O_{1.5}$ solid solution.

Figure 4. Volume fraction of reaction products in treated mixtures with $REO_{1.5}$:CMAS ratios of (a) 1:10 and (b) 1:5.

Figure 5. Schematic diagram of crystal structure and cation occupancy in (a) apatite, (b) silicocarnotite, (c) garnet and (d) diopside.

Figure 6. (a) A-B-T pseudo-ternary phase diagrams in $(Sc_xYb_{1-x})O_{1.5}$-CMAS system; (b and c) BSE micrographs of $YbSi_{0.5}O_{2.5}$/ $YbSiO_{3.5}$-CMAS mixtures treated at 1300 ^oC for 1 h